Discharge performance of a high temperature phase change material with low-cost wire mesh

Opolot, Michael; Zhao, Chunrong; Keane, Partrick F.; Liu, Ming; Mancin, Simone; Bruno, Frank; Hooman, Kamel

DOI
10.1016/j.applthermaleng.2023.120050

Publication date
2023

Document Version
Final published version

Published in
Applied Thermal Engineering

Applied Thermal Engineering 223 (2023) 120050

Contents lists available at ScienceDirect

Applied Thermal Engineering

journal homepage: www.elsevier.com/locate/ate

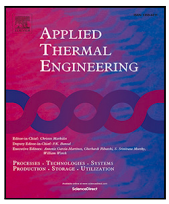

Research Paper

Discharge performance of a high temperature phase change material with low-cost wire mesh

Michael Opolot [a,*], Chunrong Zhao [a,1], Partrick F. Keane [b], Ming Liu [b], Simone Mancin [c], Frank Bruno [b], Kamel Hooman [d]

[a] School of Mechanical and Mining Engineering, The University of Queensland, QLD 4072, Australia
[b] Future Industries Institute, University of South Australia, Mawson Lakes Boulevard, Mawson Lakes, SA5095, Australia
[c] Department of Management and Engineering, University of Padova, Stradella S. Nicola, 3, Vicenza 36100, Italy
[d] Department of Process and Energy, Delft University of Technology, Leeghwaterstraat, 39 2628 CB Delft, The Netherlands

ARTICLE INFO

Keywords:
Phase change materials
Heat transfer
Experimental testing
Numerical modelling
Heat transfer enhancement

ABSTRACT

Thermal energy storage is increasingly needed in a sustainable world because of its potential of capturing waste heat and being incorporated in solar power plants. For power generation, in particular, as turbine technology advances, a demand for higher temperature thermal energy storage materials also grows. For this purpose, latent thermal energy storage fits in well since it uses phase change materials (PCMs) which generally have a higher energy density compared to their sensible heat counterparts. In the present study, a eutectic Na_2CO_3(41.69%)-(33.1%)KCl-(25.21%)NaCl phase change material (PCM) with a melting temperature of 569 °C was chosen as the storage material to experimentally assess the performance benefit of using a readily available stainless steel (ss304) wire mesh (as the periodic structure) to enhance heat transfer within the domain. In addition, for discharging, a numerical model was developed and compared with the experimental results. Furthermore, for discharging, a numerical investigation of the influence of the heat transfer fluid (HTF) flow-rate to the rate of heat transfer was performed. Overall, it was experimentally observed that the charging time for the composite case was shortened by about 35%, compared to the pure PCM case. For discharging, in the axial direction, the composite solidification time when compared to the pure PCM case was on average 10% shorter. Regarding the radial discharging performance of the composite, there was only about 5% improvement compared to the pure PCM case, which was expected due to the thermal contact resistance in the radial direction. Discharging experimental results were used to validate a discharging numerical model. Discharging results from the model showed that increasing the flow rate of the heat transfer fluid (HTF) reduced the time for solidification. It was observed that for the HTF flow rate of 5 L/min, 10 L/min, 20 L/min and 30 L/min, the discharge time was shortened by 23%, 30%, 33% and 35%, respectively.

1. Introduction

The desire to improve the reliability of renewable energy sources, particularly solar thermal energy, has resulted to a continued search for the best energy storage options that can keep solar power sources operating when the sun is down. It is evident that mature forms of energy storage for solar thermal systems are already in existence. For example, sensible heat storage is one of the mature forms of energy storage in the solar thermal spheres. The biggest challenge of sensible heat storage is the need to have large storage volumes due to their inherent low energy density [1,2]. As a result of this drawback, latent heat storage utilising a phase change material (PCM) has proven to be a promising alternative. This is due to their noticeable high energy density and isothermal discharging property that makes them perfect to maintain the heat transfer fluid (HTF) temperature at the inlet of the turbine [3,4]. PCMs have a drawback of low thermal conductivity [5,6]. However, attempts to enhance heat transfer within PCMs have been performed through the use of fins [7–10], foams [11–19], locally made periodic structures [18–22], heat pipes [23,24], encapsulation [25–27] and recently the use of additive manufacturing [28].

Steinmann et al. [29] applied a PCM-sandwich concept using graphite fins for the test storage units for the DISTOR project. Different PCMs (KNO_3-$NaNO_3$ and KNO_3-$NaNO_2$-$NaNO_3$) and fin materials

* Corresponding author.
E-mail addresses: m.opolot@uq.net.au (M. Opolot), chunrong.zhao@uq.net.au (C. Zhao).
[1] Author equally contributed as first author.

https://doi.org/10.1016/j.applthermaleng.2023.120050
Received 1 April 2022; Received in revised form 29 November 2022; Accepted 10 January 2023
Available online 14 January 2023

Nomenclature

C_p	specific heat (J/kgK)
d_f	ligament diameter (m)
d_p	pore diameter (m)
h_{sf}/H	latent heat of fusion (J/kg)
T_l	liquidus temperature (K)
T_s	solidus temperature (K)
C_i	inertial coefficient
P	pressure vector (Pa)
u	velocity vector (m/s)
b	computational constant
g	gravity (m/s^2)
h	Heat transfer coefficient (W/(m^{2}K))
HTF	heat transfer fluid
k	thermal conductivity (W/mK)
PCM	phase change material
Q	heat (J)
R	Radius (m)
T	temperature (K)
t	time (s)
TES	Thermal energy storage
V	Volume (m^3)
v	local velocity (m/s)

Greek symbols

β	thermal expansivity (1/K)
δ	infinitesimally small layer
ϵ	porosity
γ	liquid fraction
μ	dynamic viscosity (kgm^{-1}s^{-1})
ν	kinematic viscosity (m^2/s)
ω	permeability (m^2)
Φ	Mushy-zone constant (kg/m^{3}s)
ρ	density (kg/m^3)

Dimensionless numbers

Nu	Nusselt Number
Pr	Prandtl Number
Ra	Rayleigh number

Subscripts

e	effective
h	horizontal
i	initial
ins	insulation
l	liquid
m	melt
pcm	phase change material
ps	periodic structure
ref	reference
s	solid
v	vertical
w	wall

(graphite foil, aluminium, stainless steel, carbon steel and copper) were examined. Overall, no degradation was found for continuous 4000 h testing within 330 °C. Thereafter, Bayón et al. [30] further analysed the experimental behaviour of a 100kW$_{th}$ TES for direct steam generation in concentrated solar thermal power plant using this "sandwich configuration" and KNO_3-$NaNO_3$ mixture. The authors developed and demonstrated the applicability of a quasi-static model to describe the general performance of a TES system with such sandwich configurations. Furthermore, Liang et al. [31] compared graphite and steel fins with various thicknesses. The results showed that more steel fin volume was required to achieve the same heat transport performance as graphite foil, indicating a higher cost of steel fins.

Zhao et al. [32] examined the feasibility of metal foams and expanded graphite used in inorganic salt PCM. The experimental results showed that the metal forms outperformed expanded graphite, though they suffered significant surface corrosion. To realise a cost-effective performance, Zhao et al. [33] numerically investigated the performance of the inorganic PCM tank with fully/partially filled graphite foam inserts. The results exhibited the charging/discharging performance with different graphite foam porosities under fully filled scenarios. It was observed that the partially filled tank showed significant performance degradation, owing to the highly suppressed natural convection by the presence of open-cell foams.

In the present study, an attempt to use a readily available material (ss304 stainless steel woven wire mesh) to enhance heat transfer at a high temperature is carried out experimentally and a numerical prediction of the experimental data is performed. There are no studies available in the literature that have attempted to perform this kind of study. A few studies that have experimentally used a periodic structure to enhance heat transfer in PCMs have carried out their tests at low operating temperatures and there is no reporting of the numerical prediction. For example, Ebadi et al. [20] experimentally used a copper wire mesh wrapped to about 75% and 87% porosity to test the charging performance of an n-octadecane PCM. It was observed that, when a copper wire mesh was inserted, a somewhat uniform temperature is observed within the domain. In addition, as compared to the pure PCM case, a reduction in the total melting time of 17% and 25% was observed for a porosity of 87% and 75%, respectively. In another study by Righetti et al. [18], low grade aluminium mesh was used to obtain a 92% porous insert that was used to study the performance of a paraffin wax as the PCM. They concluded that a 50% reduction in the total time was realised as compared to a pure PCM case. In previous studies, using low temperature PCMs, it can be deduced that adding a periodic structure shortens the time for heat to uniformly distribute within the domain. This advantage, indirectly, reduces the total time it takes an infiltrated PCM to solidify (thus improving heat transfer) compared to the case of pure PCM. One notes that in all the aforementioned studies, that used a locally made periodic structure, the authors did not consider the paramount effect of thermal contact resistance, which was a subject of study by Opolot et al. [34]. Therefore, the performance can even be improved further if thermal contact resistance within the periodic structure is minimised through either spot welding and/or brazing to make a network of connected ligaments. At high temperature, a case in this present study, corrosion of stainless steel (after several cycles) may be an inevitable situation. This is a general challenge in dealing with high temperature PCMs [35]. An interesting study by Liu et al. [36] assessed the corrosion behaviour of stainless steel in a high temperature NaCl-Na_2CO_3 PCM for about 1000 cycles. Overall, it was observed that corrosion accelerated linearly in the first 350 cycles before stabilising at a rate of about 70 mg/cm^2. In that regard, it can be confidently asserted that stainless steel periodic structures can withstand several cycles before completely deteriorating. In addition, it is proposed that coating stainless steel with a graphite layer will not only increase the overall effective thermal conductivity, but also protect the stainless woven wire mesh from exposure to the highly corrosive PCM.

2. Problem definition

A eutectic PCM with a mixing ratio of Na_2CO_3(41.69%)-(33.1%) KCl-(25.21%)NaCl whose properties are shown in Table 1 was characterised by Liu et al. [37] as a potential PCM for high temperature latent heat thermal energy storage systems.

Table 1
Thermophysical properties PCM569 and containment material.

Property	PCM569	ss304	Insulation
Density, $\rho_{s,l}$ (kg/m^3)	2000/1700	8030	2630
Specific heat capacity, $C_{p,s,l}$ (J/kg.K)	1340/1410	502.48	1130
Thermal conductivity, $k_{s,l}$ (W/m.K)	0.6/0.5	16.27	0.07–0.18
Latent heat of fusion, H_{LF} (J/kg)	249600	–	–
Melting temperature, T_m (K)	842.15	–	–
Thermal expansion coefficient β (1/K)	0.00005[a]	–	–
Dynamic viscosity, μ (kg/m.s)	0.004	–	–

[a]Assumed based on existing literature about salts at that temperature range.

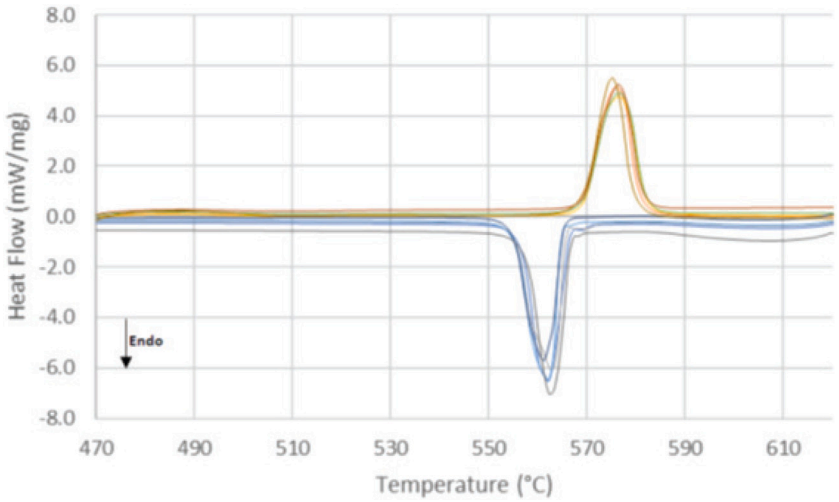

Fig. 1. DSC runs for PCM569.

The thermophysical properties of the chosen PCM were measured using a differential scanning calorimetry (DSC) (404 F1 Pegasus®, Netzsch) using five samples obtained from fresh powder PCM. Netzsch provides an evaluation software, Proteus®, which was used for evaluating the thermophysical properties of the chosen PCM. Results obtained from the characterisation of the PCM are shown in Fig. 1.

The present study attempts to understand the heat transfer mechanism within the stated PCM when a cheap and readily available stainless steel (ss304) enhancement material shown in Fig. 2 is used. One notes that Fig. 2(a) shows the properties of the mesh. Of particular interest is the understanding of the discharging cycle (how fast it can be discharged) of the already charged TES system since this will aid in determining the TES effectiveness. In addition, numerical predictions of the experimental data is explored to give an overview of how heat losses, if not experimentally captured, at such high temperatures impact the numerical predictions. Furthermore, a parametric study of the effect of HTF flowrate to the overall heat transfer process and solidification of PCM is performed.

3. Part A: Experimental approach

3.1. Experimental setup

The experimental rig shown in Fig. 3 was constructed from stainless steel (grade ss304). The heat trace element (1.05 kW) was wrapped at the bottom part of the constructed rig up to 300 mm (See Fig. 4(a)) to provide external heating of the PCM up to when it fully melts. Twelve K-type thermocouples (T01–T12) with an accuracy of ±2 °C were first calibrated before installing in the respective locations of the tank as shown in Fig. 4(b). These thermocouples were then connected to the data logger (DT85 W DataTaker) which were later monitored from the DeLogger software installed in the control computer.

Two extra thermocouples, T13 and T14, were connected to the heat trace (see Fig. 4(b)). T14 is taken to be the representative temperature of the heat trace and it is the one that the Eurotherm temperature controller uses as the reference temperature when ramping up the temperature of the domain. On the other hand, T13 is the over temperature thermocouple (safety set-point upon which the Eurotherm temperature controller cuts-off power supply to the heat trace once reached). For this study, T14 was set at 700 °C while T13 at 800 °C. One notes that these two thermocouples (T13 and T14) were not connected to the data logger. However, T01–T04 were at the outer diameter of the outer pipe, thus giving the real temperature at the domain wall. One also notes that T12 was connected at the same location with T13 and T14 (see Fig. 4(b)) as a spare over temperature thermocouple in case T13 failed during operation.

In order to determine how much energy is consumed by the heat trace to raise the temperature of the domain, the pulse metre was connected between the temperature controller and the heat trace (see Fig. 4(b)). The pulse metre was calibrated to deliver an impulse for every 10Wh consumed by the heat trace. This way, the total cumulative power consumed by the heat trace can be calculated to achieve and maintain the set temperature.

The next step was to apply the bottom and radial insulation as shown in Figs. 3(b) and 3(d). About 200 mm in thickness of calcium silicate sheets were placed at the bottom of the tank. Similarly, about 200 mm of ceramic fibre was wrapped around the tank. Before the top part of the tank was covered and insulated, 4.86 kg of powder PCM was poured into the tank domain whose height was 335 mm (obtained by deducting the top empty height from the actual tank height). A high temperature adhesive glue was applied around the top cover in order to keep the whole tank airtight. The argon gas and air lines were then connected to complete the entire assembly (argon gas was used as a sealant to prevent the PCM exposure to the atmospheric air. Also, because of its low thermal conductivity, it acted as an insulation layer on top of the PCM.) Finally, 200 mm of ceramic fibre insulation was placed on top to fully insulate the tank domain. The final experimental

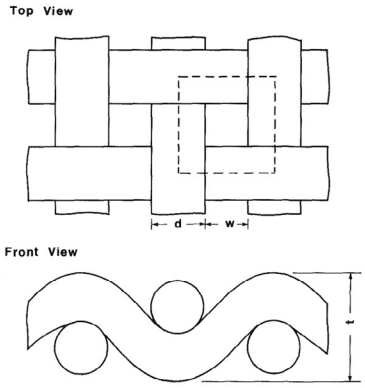

(a) Wire screen standard layout [38]. For this study, d = 1.6mm, w = 5.2mm while t = 3.2mm and the open area is 67%

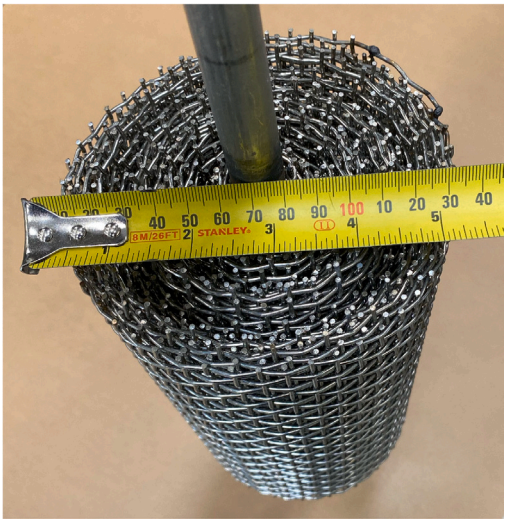

(b) Top view of experimental Periodic structure

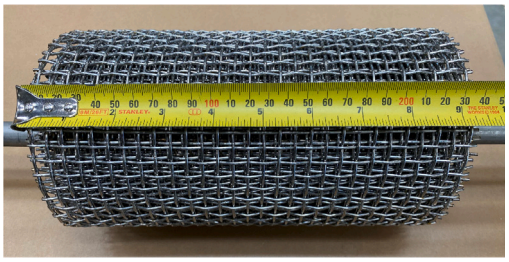

(c) Side view of experimental Periodic structure

Fig. 2. Periodic structure with a measured porosity of 80% used in the experimental study[38].

lab setup is shown in Fig. 3(d). Note that the same procedure was applied for the periodic structured tank.

At this stage, the experimental rig was ready for the first step of melting the powder PCM in order to properly mix the constituents of the PCM and also to infiltrate the periodic structure (for the case of the enhanced tank). Melting of the PCM from its powder form was performed to make its ingredients completely mix. This was done by setting the heat trace controller temperature to 700 °C at a ramping rate of 0.3 °C/min. After all the thermocouples read a minimum temperature of 650 °C (which is above the melting point of the PCM), the PCM in the domain was believed to have completely melted and a mixture of ingredients realised. The heat trace was then switched off and the PCM was allowed to naturally cool down to 20 °C. In order to observe the newly solidified PCM, the top insulation and cover was removed to inspect the new solid PCM that was ready for cycling tests. The inspection was done, in part to determine the new height of the PCM as compared to that of powder PCM height and also to ascertain that the final PCM was in solid state.

Once initial PCM melting was performed, the actual cycling of PCM was performed by charging the PCM using the heat trace. The heat trace heating was ramped up at a rate of 130 °C/min up to when the controller set temperature of 700 °C was reached. This high ramping rate was to ensure that the heat trace delivered its maximum energy of 1.05 kWh, such that a consistency in energy input is observed across all the cycles. Once it reached to 700 °C, the heat trace controller held this temperature up to when the lowest temperature of the thermocouple in the storage tank registered a minimum temperature of 609 °C (T09). At this point it was assumed that the charging cycle ended since the whole PCM in the domain melted and it was only sensible heat addition taking place. A transition to discharging was initiated by, first, turning off the heat trace and then flowing air at room temperature (27 °C) with a controlled volumetric flow rate of 5 L/min through the HTF pipe of the domain. The discharging cycle was ended when the final thermocouple reaches to 450 °C (T05) and at this point, it was assumed that the entire PCM in the domain solidified. The procedure was then repeated by initiating the charging cycle, first, by turning off the air flow and secondly, by turning on the heat trace controller to deliver energy to the heat trace. This procedure was repeated (both in pure PCM and infiltrated cases) for two cycles of charge–discharge.

Table 2
Instrumental accuracy.

Equipment	Uncertainty
K-type TCs	± 2 °C
Air flow metre	± 0.05 L/min
DT85 W DataTaker	±0.01 °C
Electrical energy (Wh)	± 10 Wh

3.2. Experimental uncertainty

Experimental errors may result from thermocouples' (TCs) calibration (the K-type thermocouples used were calibrated, with accuracy of 2 °C), air flow metre with an accuracy of 0.05 L/min, heat trace eurotherm controller uncertainty of 1 °C, DT85 W DataTaker data logger with an accuracy of 0.01 °C while the electrical energy can be taken to have uncertainty of a pulse, which measured 10 Wh. Table 2 shows the summary of the uncertainty tolerated in the experiments.

3.3. Energy balance

In the overall cycle (see Fig. 5(a)), the heat trace that was used to melt the PCM delivered a total amount of heat that was used to melt the

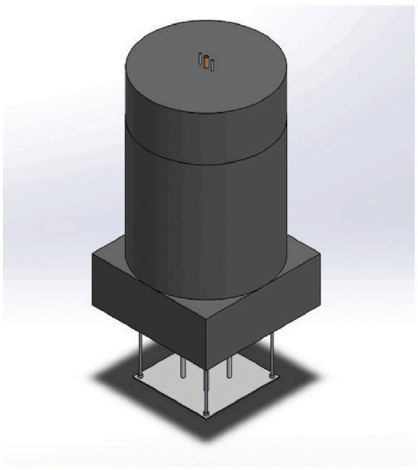

(a) Isometric view

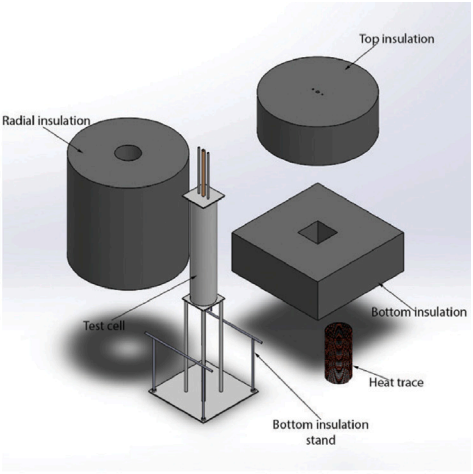

(b) Exploded view

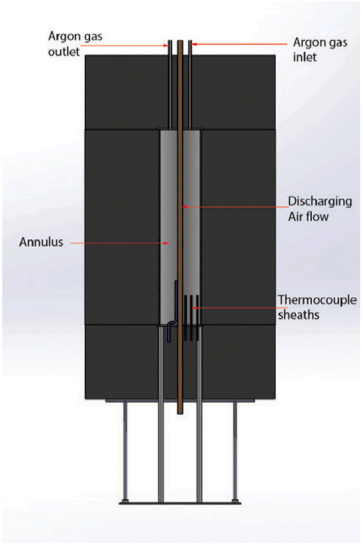

(c) Front cross section view

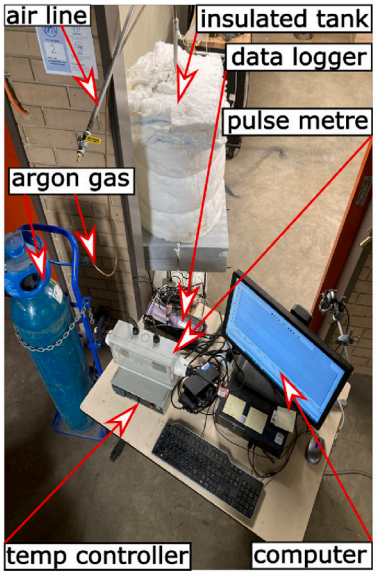

(d) Lab set up

Fig. 3. Experimental tank 3D model and actual lab set up.

PCM while a certain proportion was stored in the insulation material, tank material, periodic structure and in the PCM as sensible energy. In addition, a part of it was lost to the environment with time through conduction, convection and radiation. Theoretically, three forms of heat addition to the PCM are realised, that is, initial sensible heat addition, latent heat absorption due to a phase changing process and finally, sensible heat addition due to overheating beyond the melting point of the PCM while at the same time heat is stored in the insulation and also lost to the environment at a certain rate depending on the insulation and the ambient conditions. Theoretically, Eq. (1) gives the total initial steady state energy stored (at t = 0, T = 665 °C and the charging cycle is considered to start from 500 °C) in the control volume at the end of the charging process.

During discharging (see Fig. 5(b)), the overall heat stored within the control volume (as shown in Eq. (1), where heat lost, stored in insulation and tank material during charging is not accounted for) will be absorbed by the HTF while the rest is lost as heat losses to the surrounding as shown in Eq. (2). It is worth noting that the heat transfer process in the PCM undergoes three stages, namely, early sensible heat rejection, latent heat rejection and finally, sensible heat rejection during over cooling. The portions of energy lost during discharging can be obtained using Eq. (4), where the heat transfer coefficient during convective heat losses around the radial insulation is estimated using Eq. (5) [39] and that of the top and bottom insulation is estimated using Eq. (6) [40].

$$Q_{ini} = \sum m_{ps} C_{p,ps} \bar{T} + m_{PCM} C_{p,PCM} (T_{melt} - 500) + m_{PCM} C_{p,PCM} (665 - T_{melt}) + \frac{1}{3600} m_{PCM} h_{sf} \quad (1)$$

$$Q_{ini} = Q_{HTF} + Q_{loss} \quad (2)$$

$$Q_{HTF} = \sum_{j=0}^{j=n} \dot{m}_{HTF} C_{p,HTF} (T_{out} - T_{in}) \quad (3)$$

$$Q_{heat\text{-}loss} = \frac{1}{3600} \sum_{j=1}^{j=n} h_{ins\text{-}radial} A_{ins\text{-}radial} (T_{ins\text{-}radial,j} - \bar{T}_{air,j}) \Delta t_j + \frac{1}{3600} \sum_{j=1}^{j=n} h_{ins\text{-}top} A_{ins\text{-}top} (T_{ins\text{-}top,j} - \bar{T}_{air,j}) \Delta t_j + \frac{1}{3600} \sum_{j=1}^{j=n} h_{ins\text{-}bottom} A_{ins\text{-}bottom} (T_{ins\text{-}bottom,j} - \bar{T}_{air,j}) \Delta t_j + \frac{1}{3600} \sum_{j=1}^{j=n} \epsilon \sigma A_{local} (T_{local,j}^4 - \bar{T}_{air,j}^4) \Delta t_j \quad (4)$$

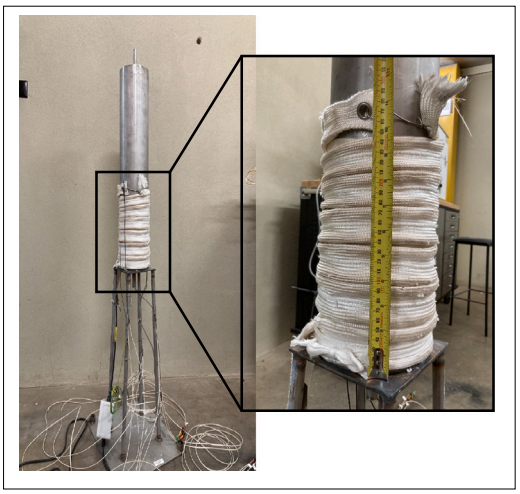

(a) 1.05kWh heat trace location and length

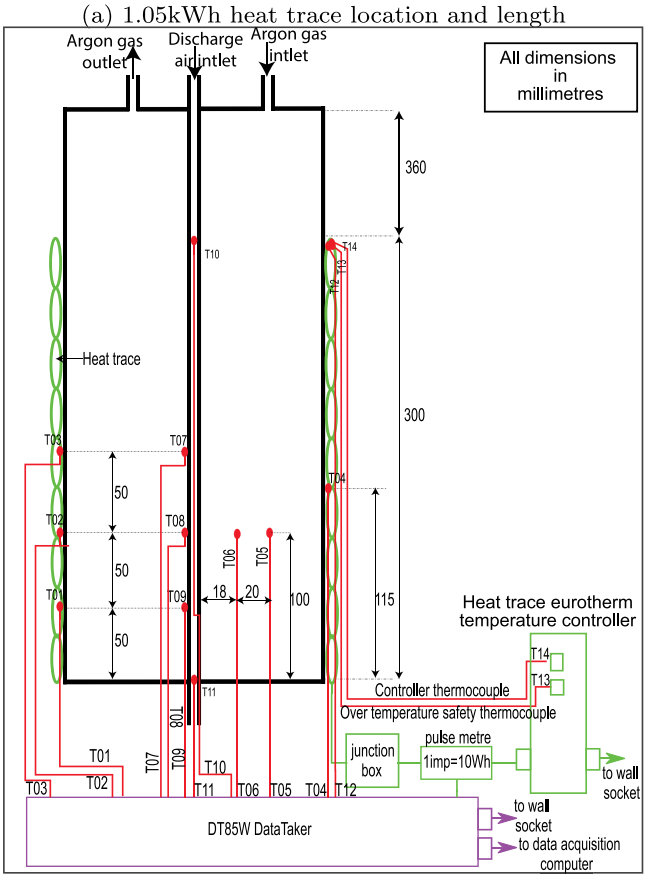

(b) Thermocouple and connection schematic

Fig. 4. Heat trace and thermocouple map.

$$h_{radial} = \bar{N}u_v \frac{k_{air}}{L_v} = \left\{ 0.68 + \frac{0.67Ra_v^{\frac{1}{4}}}{\left[1 + (\frac{0.492}{Pr})^{\frac{9}{16}}\right]^{\frac{4}{9}}} \right\} \frac{k_{air}}{L_v} \quad (5)$$

$$h_{top\text{-}bottom} = \bar{N}u_h \frac{k_{air}}{L_h} = \left[0.54Ra_h^{\frac{1}{4}}\right] \frac{k_{air}}{L_h} \quad (6)$$

To show where the heat loss from the experimental setup is the highest, Fig. 6 shows some of the infra-red images that were captured during experiments. It can be seen that heat was lost through some pockets in the insulation, for example, where the thermocouple sheaths protrude from and at joints of different insulation layers.

However, for this study, the interest is to know what proportion of the initial energy was absorbed by the HTF during the discharging cycle while the heat lost to the surrounding will be a lumped value (not distinguished in its different forms of heat loss like conduction, convection and radiation heat losses). For this purpose, numerical analysis was used to estimate the percentage of energy to the HTF. In order to achieve this, a numerical model was run when heat losses are accounted for and another model was run when 100% of the initial energy is absorbed by the HTF (when the control volume is adiabatic). In this case, the proportion of energy (lumped value) that was lost to the surrounding can be obtained as the difference between the two numerical cases. Section 4.4 gives the results obtained in the numerical energy balance estimation.

3.4. Preliminary experimental results

The initial melting and cooling results showed that the PCM melted and solidified in both the pure PCM case and the composite case as shown in the thermocouple temperature readings in Figs. 7(a) and 7(b). To further confirm this, a closer look at the inside thermocouples (T05, T06, T07 and T08) temperature reading shown in Fig. 7(c) & 7(e) for pure PCM case and Fig. 7(d) & 7(f) for composite case shows that a phase change process occurred in the range of 569–571 °C. One notes that there is a temperature fluctuation during a transition from powder to liquid for the composite case. This is attributed to the fact that, as the powder PCM melts, the liquid PCM infiltrates the periodic structure and a noticeable fluctuation in temperature can be observed (see Fig. 7(d)). It can, therefore, confidently be assumed that the ingredients of the PCM uniformly mixed and got infiltrated into the periodic structure (for the case of the composite) since both melting and solidification transition points occurred at nearly the same temperature range.

In order to view the newly solidified PCM, the top insulation and cover were removed and the appearance of the PCM when initially in its powder form and the final solidified form was observed as shown in Fig. 8(a) while the infiltrated mesh was observed as shown in Fig. 8(b). Measurement of the heights of the new solidified PCM domain and the infiltrated mesh were observed to be 190 mm and 237 mm respectively. The tanks were again covered and the top insulation placed back in order to re-warm the domain before performing the actual charging–discharging cycling.

The objective of re-warming the PCM was to ideally reach the initial boundary condition of 500 °C and a final internal temperature of at least 665 °C at the end of the charging cycle. In order to achieve this, the PCM was charged at a temperature rate of 130 °C/min up to when the lowest thermocouple reading was 610 °C.

3.5. Final experimental results

The actual charging–discharging cycling of the PCM was then performed at a heat trace set temperature of 700 °C. Fig. 9 shows the repeatability of the charge–discharge cycling of both pure PCM and the composite cases. It can be observed that charging and discharging occurred at the same transition temperature of the chosen PCM. Furthermore, it is observed that inserting the wire meshes improves the overall cycle performance by about 10%.

Experimental repeatability was first assessed to demonstrate the reliability of the thermocouple sensors after several cycles. Since the PCM transition temperature was in the range of 569–571 °C, results were reported for a temperature range of 665 °C–500 °C, whereby, the focus was to determine how long it took PCM569 to fully solidify.

Thermocouple T05 was chosen to show the repeatability of both pure PCM and composite cases as shown in Fig. 9(a), 9(b), 10(a) & 10(b) where an acceptable repeatability is observed.

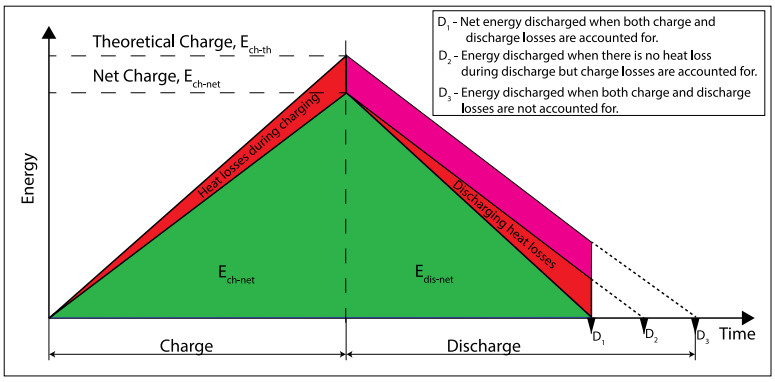

(a) Charge-discharge energy storage balance

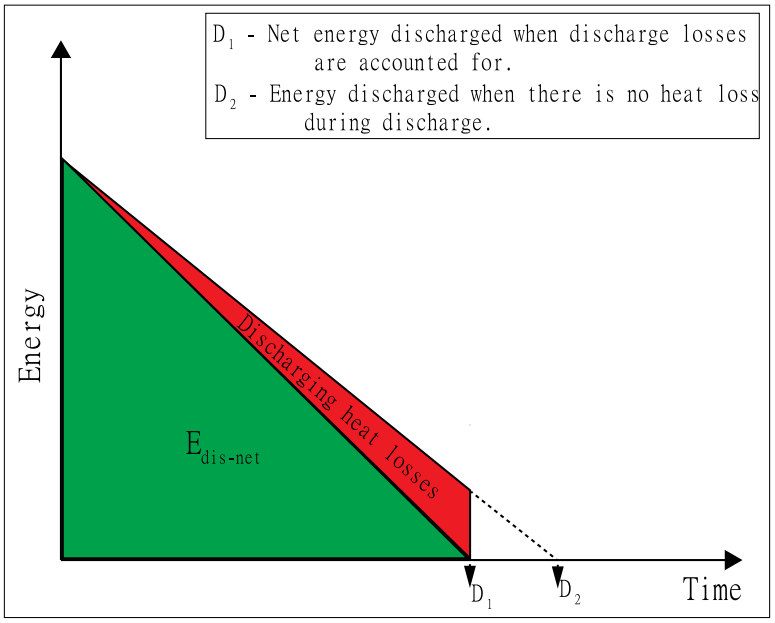

(b) Discharge energy storage balance

Fig. 5. Theoretical energy balance (the process may not be linear).

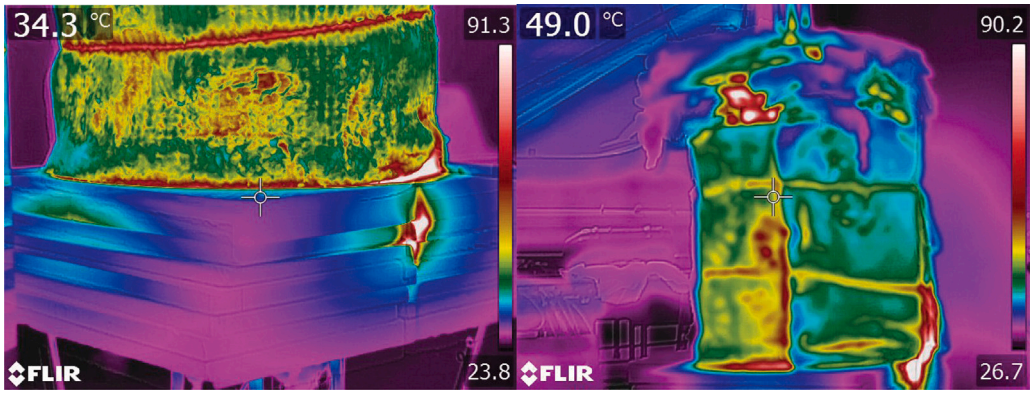

Fig. 6. Thermal images showing high temperature spots.

Although, stainless steel (ss304), which in this case is the woven periodic structure enhancing heat transfer, is prone to corrosion (in salt conditions) and has a poor thermal conductivity, as compared to graphite, copper and aluminium foams, at least an overall improvement in the system performance was observed. It should be noted that woven meshes, when infiltrated in a fluid, result to a low effective thermal conductivity as compared to tetrakaidecahedron metal foams. This is in part attributed to their high open porosity and the tortuosity effect [41].

Results pertinent to the charging process (see Fig. 11) for both pure PCM and composite cases show that charging time for the latter case is shortened by about 35%, compared with the former. Approximately a 20 min respond time is noticed beyond which the thermocouples register an increase in the PCM temperature. The effect of the periodic

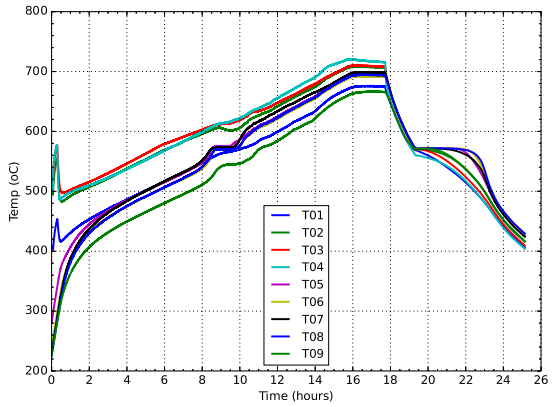

(a) Pure PCM all thermocouple readings

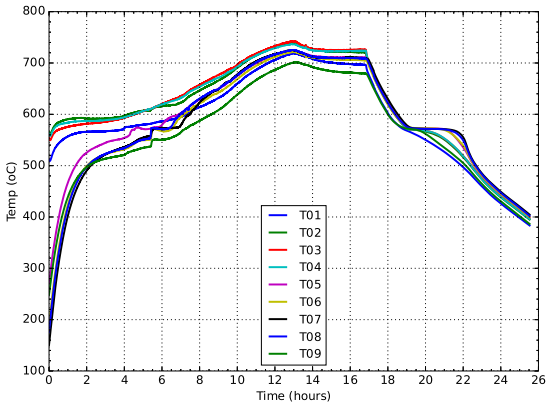

(b) Composite all thermocouple readings

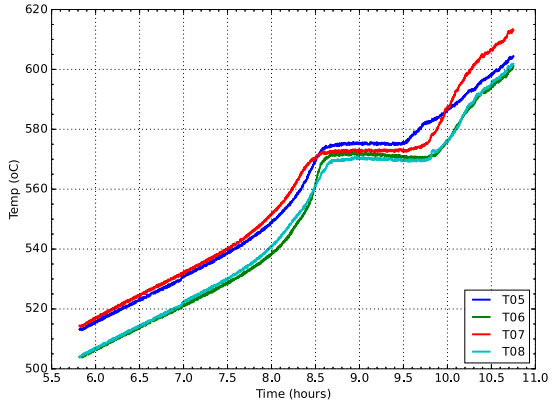

(c) Pure PCM melting transition

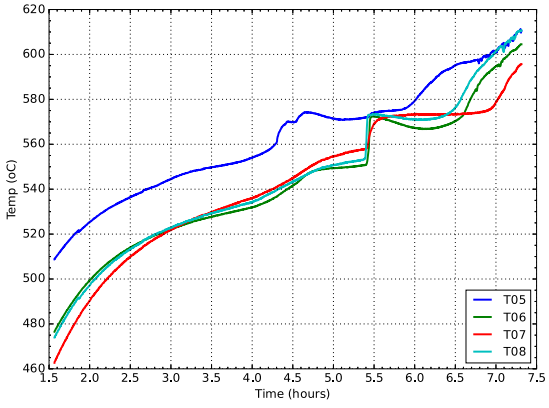

(d) Composite melting transition

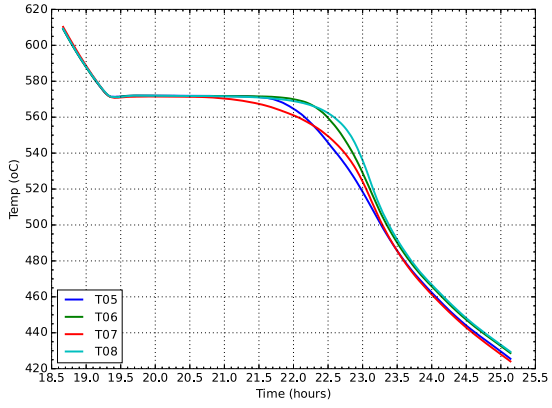

(e) Pure PCM solidification transition

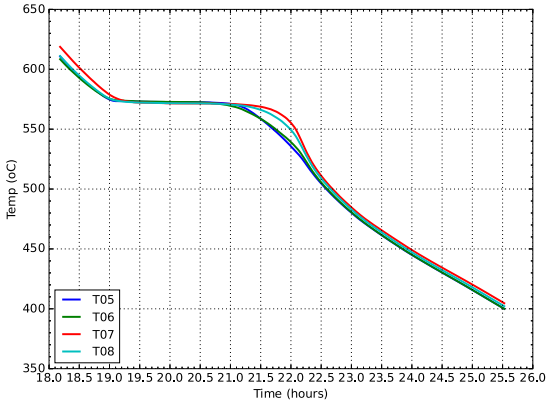

(f) Composite solidification transition

Fig. 7. Preliminary melting and solidification of both pure PCM and composite cases.

structure is realised in the early stages of charging when the PCM is still in solid state, presumably due to accelerated conduction attributed to the network of periodic wire meshes in the domain.

The temperature profiles in Fig. 11(c) are more bundled during the phase transition, between 1–1.5 h, except for the axial temperature variation as demonstrated in Fig. 11(d). When a phase change transition is realised, the periodic enhancement effect is not noticed. However, after a transition state is completed, the periodic structure further promotes heat transfer within the domain, thus accelerating the charging process. As seen, just after about 1.5 h of charging, the temperature response is much faster for the composite case as compared with that of pure PCM. After 2 h, the radial temperature profiles, as depicted in Fig. 11(c), stand between 670–685 °C while those of pure PCM are starting to cross the 670 °C line only after 2.5 h. As seen, the composite structure works better and charging time is shortened by 35%compared with that of pure PCM.

For the discharging part of the cycle, the observed behaviour of temperature distribution within the domain (see Fig. 12) shows conduction is the main heat transfer mechanism in solidification of PCM. The composite case performs much better than the pure PCM case because the periodic structure enhances heat conduction from the PCM to the HTF. At the early stage of solidification (sensible heat rejection), there

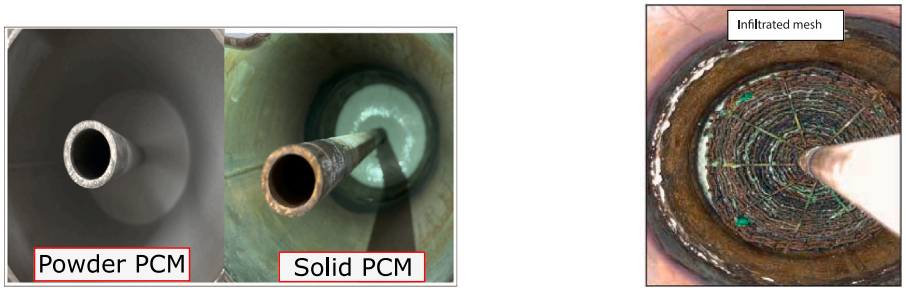

(a) Pure PCM case (b) Composite case

Fig. 8. Initial melting & solidification of PCM for both pure PCM and composite cases.

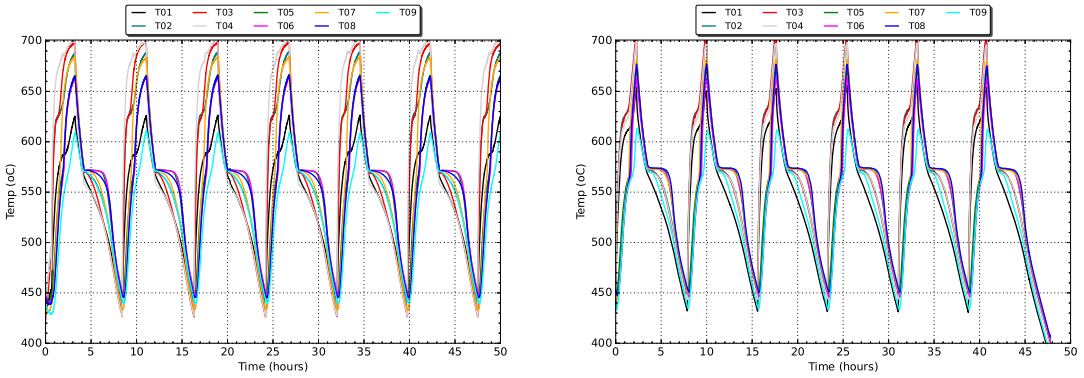

(a) Pure PCM charge-discharge case repeatability (b) Composite charge-discharge case repeatability

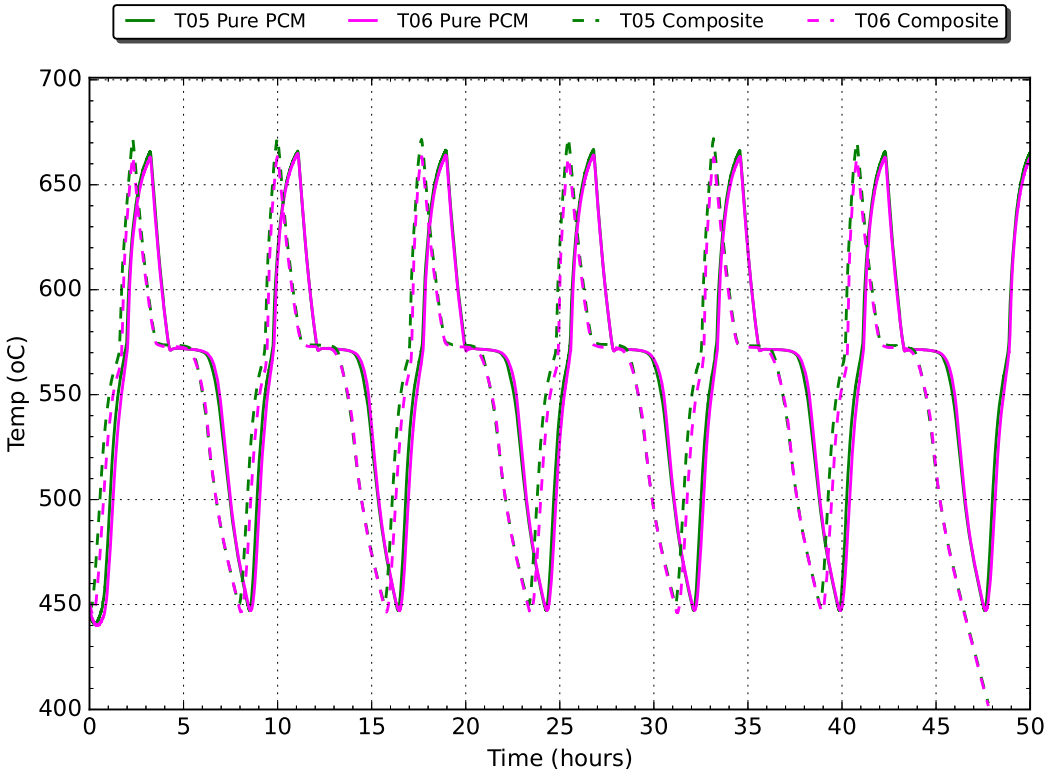

(c) Pure PCM and composite cycling comparison

Fig. 9. Total testing time and repeatability of the experiment.

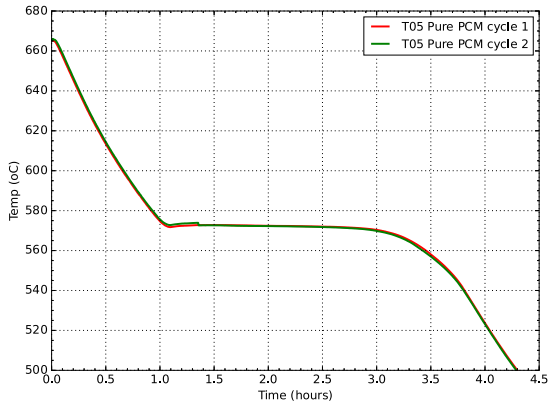

(a) Pure PCM discharge case repeatability

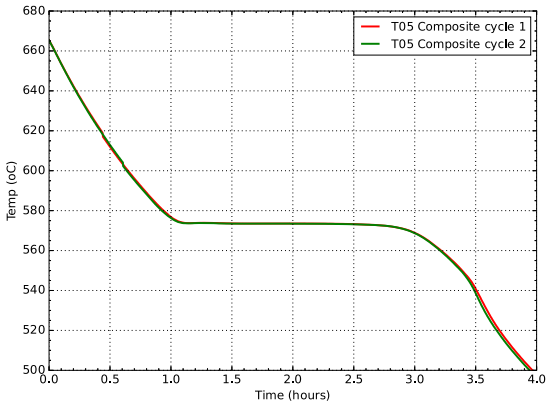

(b) Composite discharge case repeatability

Fig. 10. Pure PCM case vs composite case repeatability test.

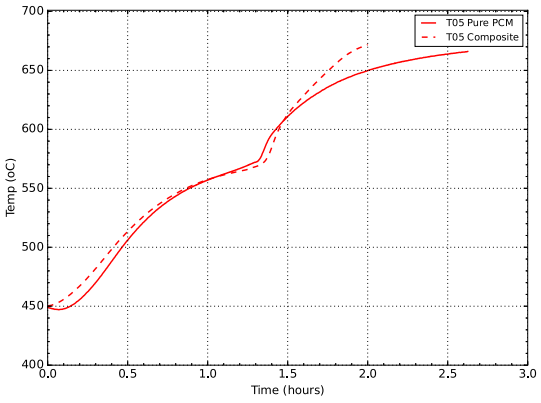

(a) T05 Centre temperature variation comparison

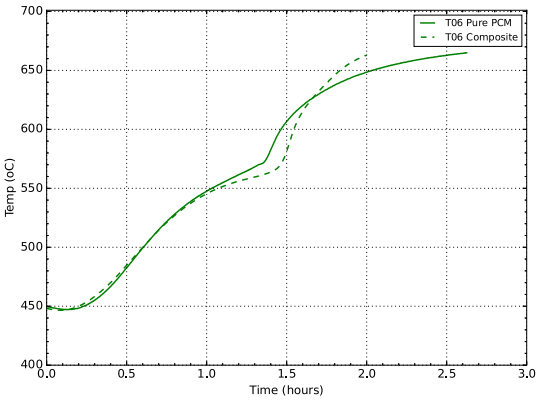

(b) T06 Centre temperature variation comparison

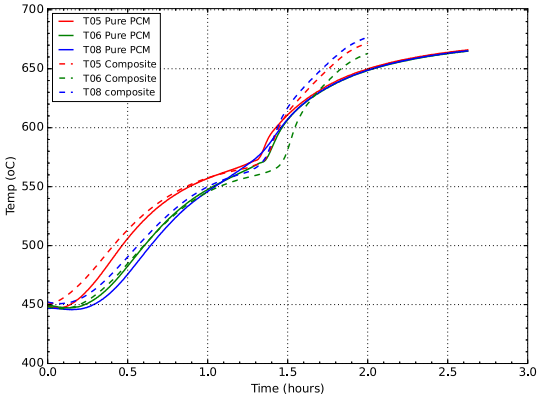

(c) Radial temperature variation comparison

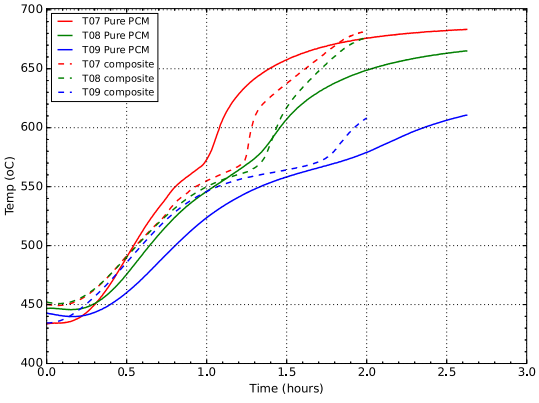

(d) Axial temperature variation comparison

Fig. 11. Pure PCM vs composite case during charging.

is a slight noticeable change in the rate of solidification as compared to the pure PCM case. This is because, at this early sensible heat rejection, convection (see [42]) is the dominant heat transfer mechanism which would render the periodic structure as a hindrance in the convection cell formation. However, a relatively small heat conduction through the periodic structure contributes to the heat transfer process which is not witnessed in the pure PCM case. In the second stage of heat rejection, a latent heat rejection is observed where the PCM is a mixture of both phases (the mushy zone). As the third stage approaches (another sensible heat rejection), the proportion of solid PCM within the domain outweighs that of the liquid form. In this scenario, the benefit of the periodic structure in enhancing heat conduction is observed. At this point, an early completion of latent heat rejection is observed in the composite case compared to pure PCM and an even significant benefit is realised after a complete latent heat rejection, where conduction is the sole heat transfer mechanism remaining. It is, therefore, clearly observed that enhancing the PCM promotes heat transfer by conduction within the domain.

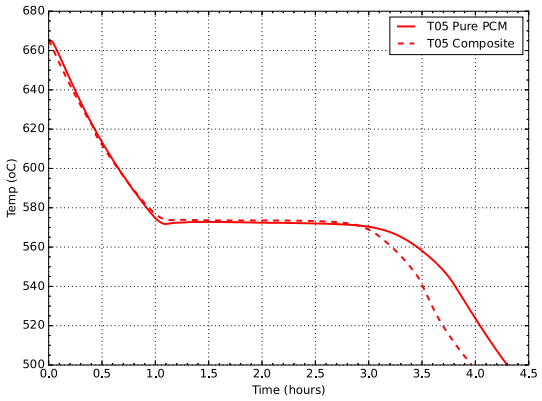

(a) T05 Centre temperature variation comparison

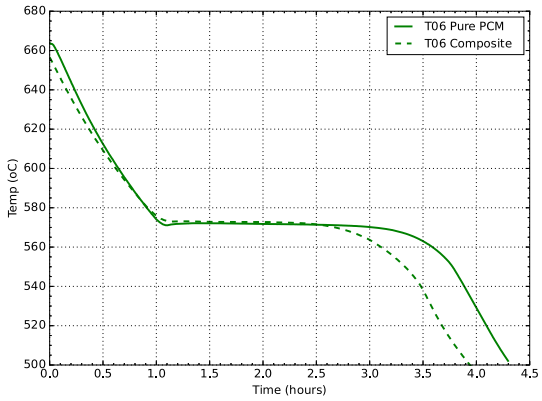

(b) T06 Centre temperature variation comparison

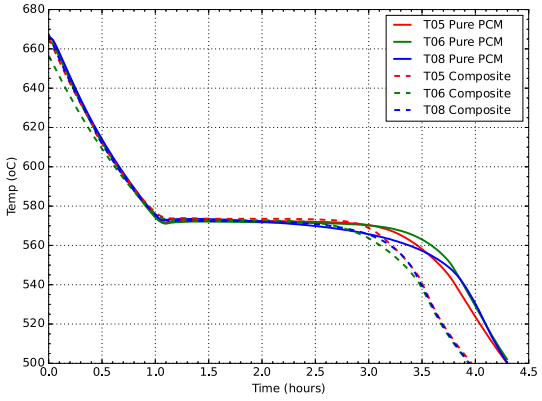

(c) Radial temperature variation comparison

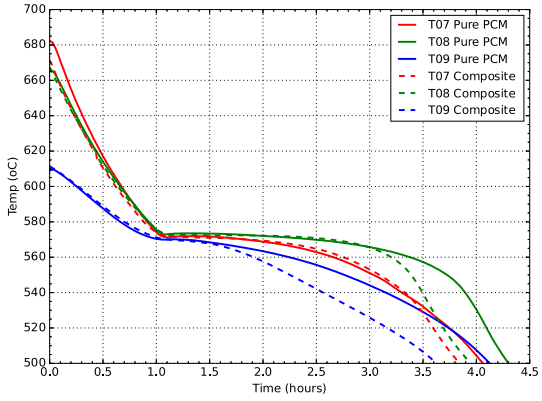

(d) Axial temperature variation comparison

Fig. 12. Pure PCM vs composite case during discharging.

On the choice of using stainless steel periodic structures, one should note that, at such a high operating temperature of PCM (which is the case for concentrated solar power plants), aluminium and copper foams are not suitable (although they are corrosion resistant). This is because aluminium and its alloys' melting point is in the range of 400 °C-700 °C. Although copper, on the other hand, melts at about 1100 °C, it loses its properties as temperature increases. In that regard, the choice of using stainless steel as the periodic structure can be validated because it is cheap and readily available compared to graphite (the best alternative at this operating temperature range).

Fig. 12 shows a comparison of the performance of both pure PCM and the composite. Overall, results show that an improvement in performance was realised where an early solidification is obtained in the composite case. Looking at a comparison of thermocouples T05 and T06 shown in Figs. 12(a) and 12(b) respectively, one observes an even higher performance enhancement closer to the HTF pipe. For example, using T06 (see Fig. 12(b)), an earlier completion of latent heat rejection is noticed in the composite case compared to the pure PCM case. The same phenomenon is further demonstrated in Fig. 12(c) which shows the radial temperature variation for both the composite and pure PCM cases.

A closer look at Fig. 12(d) that shows the axial variation of temperature, it is noticed that the time it takes the composite to fully solidify compared to the pure PCM case is about 15% shorter when looking at the bottom thermocouple (T09), about 10% in the middle (T08) and around 8% in at the top of the domain (T07). This phenomenon demonstrates that having a periodic structure aids in speeding up the solidification at the bottom of the tank due to the dominance of heat conduction in the domain which is attributed to the periodic structure. It can further be observed that having a periodic structure in the domain leads to a relatively uniform temperature as opposed to stratification which might be observed in the pure PCM case. A look at the radial performance of the composite as compared to the pure PCM case, one observes a relatively small improvement in performance of about 5%. This trend was expected in this experimental test based on how the periodic structure was wrapped. Ideally, there was a thermal contact resistance (due to the discontinuation of the periodic structure) along the radial direction as opposed to the axial direction. The small improvement in performance along the radial direction can be attributed to the localisation of temperature within the pores of the periodic structure.

4. Part B: Numerical approach

4.1. Mathematical formulation

In this study, the domain shown in Fig. 13 is symmetrically subjected to numerical studies. Using the domain in Fig. 13, which is a conjugate heat transfer problem between the solidifying PCM in the annulus and the flowing HTF in the inner pipe, an attempt to generate a simple model that uses a fixed grid approach is undertaken. Firstly, the numerical formulation of the PCM domain is performed, which is closely followed by the HTF numerical formulation before a conjugate heat transfer coupling through the interface wall is mentioned.

For the PCM part of the domain, enthalpy-porosity method is used. In the numerical analysis, it is assumed that the PCM behaves as an in-compressible Newtonian fluid when in liquid form. In addition, for

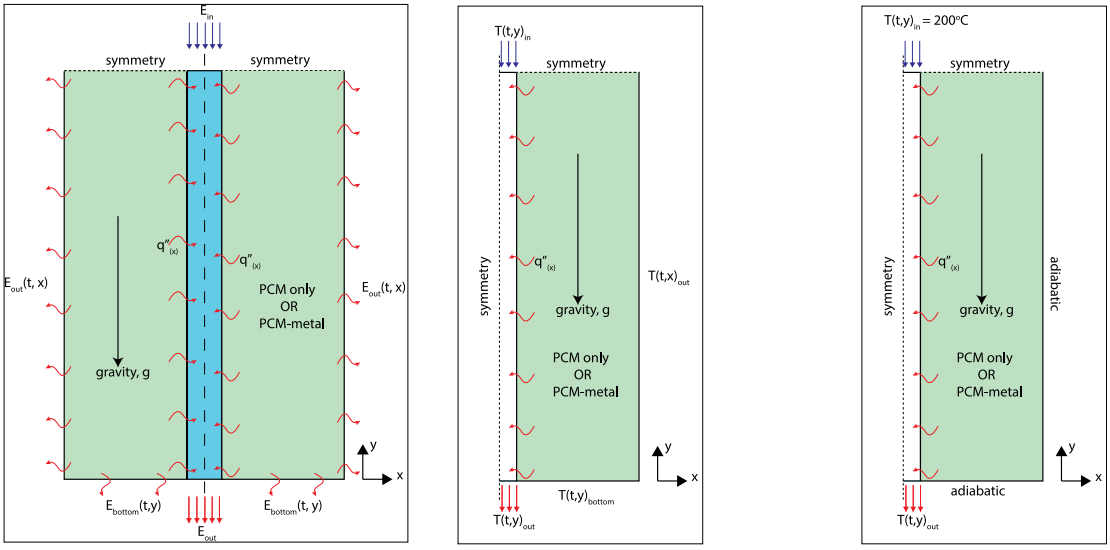

(a) Energy balance for experimental studies

(b) Numerical model for experimental data comparison

(c) Numerical model for parametric study

Fig. 13. Numerical domain for both Pure PCM case (Height, H = 190 mm, Radius, R = 67.25 mm) and composite case (Height, H = 237.5 mm, Radius, R = 67.25 mm).

simplicity in numerical studies, the Boussinesq approximation is considered for buoyancy driven flows and a no-slip condition at the walls is considered to be valid for this study. For the PCM infiltrated periodic structure, it is assumed that the periodic structure is isotropic and exhibits constant thermophysical properties. An understanding of the enthalpy-porosity model used in this study can be found in Refs. [43–46]. The enthalpy-porosity method is well known to fairly predict the heat transfer mechanism in PCMs with either a single point melting temperature or with a melting temperature range [47]. In addition, the enthalpy-porosity method uses a volume tracking scheme on a fixed grid which eliminates the intricacy of tracking a non-linear melting front [48,49]. Based on those advantages, ANSYS Fluent 19.2®, which uses the enthalpy-porosity method, was used to solve a 2D symmetric numerical code for the chosen domain shown in Fig. 13. The general governing equations shown in Eq. (7), (8) and (9) were then used to solve the PCM domain. In the governing equations, the constant, **F**, is taken to be unity for the PCM/the porous media domains and zero for the HTF domain. In addition, for the pure PCM case, the last term on the right of Eq. (8) is dropped while the porosity, ϵ in Eq. (9) is taken to be unity.

$$\nabla.\mathbf{u} = 0 \tag{7}$$

$$\rho\frac{\partial \mathbf{u}}{\partial t} + \rho\mathbf{u}.\nabla\mathbf{u} = -\nabla\mathbf{P} + \mathbf{F}\rho\mathbf{g}\beta(\mathrm{T}-\mathrm{T}_{\mathrm{ref}}) + \mu\nabla^2\mathbf{u} - \mathbf{F}\frac{\boldsymbol{\Phi}}{\rho}\frac{(1-\gamma)^2}{(\gamma^3+\mathrm{b})}\mathbf{u} - \mathbf{F}\left(\frac{\mu}{\omega} + \mathrm{C_i}\frac{\rho|\mathbf{u}|}{\sqrt{\omega}}\right)\mathbf{u} \tag{8}$$

$$[\epsilon\rho(\gamma\mathrm{C_p} + (1-\gamma)\mathrm{C_p}) + ((1-\epsilon)\rho\mathrm{C_p})]\frac{\partial \mathrm{T}}{\partial \mathrm{t}} + (\rho\mathrm{C_p})\mathbf{u}.\nabla\mathrm{T} = \mathrm{k}\nabla^2\mathbf{T} - \mathbf{F}\epsilon\rho\Delta\mathrm{H}\frac{\partial\gamma}{\partial \mathrm{t}} \tag{9}$$

$$\gamma = \begin{cases} 0 & \text{if} \quad \mathrm{T} \le \mathrm{T_S} \quad \Longrightarrow \text{Solid;} \\ \frac{\mathrm{T}-\mathrm{T_S}}{\mathrm{T_L}-\mathrm{T_S}} & \text{if} \quad \mathrm{T_S} \le \mathrm{T} \le \mathrm{T_L} \quad \Longrightarrow \text{Mushy region;} \\ 1 & \text{if} \quad \mathrm{T} \ge \mathrm{T_L} \quad \Longrightarrow \text{Liquid.} \end{cases} \tag{10}$$

In order to model the porous media in a PCM, the last term in Eq. (8) contains the permeability coefficient, ω, and the inertial coefficient, C_i. These coefficients are estimated using the correlations developed by Hooman and Dukhan [50] as shown in Eq. (11) and (12), respectively. On the other hand, in order to determine the pore diameter of the enhancement periodic structure, the ratio of ligament diameter to pore diameter correlation formulated by Tamayo & Hooman [51] as shown in Eq. (13) was utilised. The Mushy-Zone constant, $\boldsymbol{\Phi}$ in the second last term of Eq. (8) was taken to be 10^5 and was good enough to lead to a zero velocity while the constant b in the same term was taken to be 0.001 to generally avoid a division by zero when a transition from liquid to solid is realised during heat addition and removal from the PCM.

$$\omega = 0.054\mathrm{d_p^2}\epsilon\sqrt{(1-\epsilon)} \tag{11}$$

$$C_i = \frac{0.233\left(\frac{1-\epsilon}{\epsilon^6}\right)^{\frac{1}{4}}}{\sqrt{\omega}} \tag{12}$$

$$\frac{\mathrm{d_f}}{\mathrm{d_p}} = 1.18\sqrt{\frac{1-\epsilon}{3\pi}}\left(\frac{1}{1-e^{\frac{-(1-\epsilon)}{0.04}}}\right) \tag{13}$$

A thermal equilibrium numerical code was set up for this study. According to Mahdi et al. [52], there is no noticeable difference between a thermal equilibrium and a non-equilibrium method. This, therefore, justifies the use of thermal equilibrium modelling in this present study. In that regard, the numerical solver was set up as a fully implicit scheme with a SIMPLE (semi-implicit method for pressure linked equation) algorithm [53] to handle the pressure-velocity coupling. Pressure correction was handled by the PRESTO! scheme whereas the QUICK scheme solved the convection–diffusion terms of the governing equations.

Once the numerical code is validated using the pure PCM experimental data, the porous media model that was previously validated in Refs. [34,54] was used to predict the performance of the periodic structure case. The porous media model requires the prediction of the effective thermal conductivity of the infiltrated periodic structure (ss304), whose thermophysical properties are shown in Table 1. One notes that, of paramount importance is an accurate prediction of the effective thermal conductivity, k_e, when the periodic structure shown in Fig. 2 is introduced into the PCM to cheaply enhance heat transfer and thus shorten the discharging time of the energy storage tank.

Table 3
Discharging numerical study initial and boundary Conditions.

Case	Inlet	Outlet	Outer wall	Bottom wall	Initial conditions
Validation	$T_i(t)$, v = −0.557 m/s	pressure outlet	$T_o(t)$[a]	$T_b(t)$[a]	938.15 K at t = 0
Parametric	T_i = 200 °C, v = −0.557 m/s	pressure outlet	adiabatic	adiabatic	938.15 K at t = 0
	T_i = 200 °C, v = −1.114 m/s	pressure outlet	adiabatic	adiabatic	938.15 K at t = 0
	T_i = 200 °C, v = −2.229 m/s	pressure outlet	adiabatic	adiabatic	938.15 K at t = 0
	T_i = 200 °C, v = −3.349 m/s	pressure outlet	adiabatic	adiabatic	938.15 K at t = 0

[a]Refer to Section 4.2 for the polynomial equations.

Models have been developed and experimentally validated to predict the effective thermal conductivity of an interconnected tetradecahedron periodic structures infiltrated with a fluid. A study by Ranut [55] reported some of such correlations and their comparison to experimental data. In this study, a model developed by Mesalhy et al. [56] as shown in Eq. (14) was utilised to estimate the effective thermal conductivity of the PCM infiltrated periodic structure, assuming it were an interconnected tetradecahedron periodic structures.

$$k_{eff} = \frac{\left[k_{pcm} + \pi\left(\sqrt{\frac{1-\epsilon}{3\pi}} - \frac{1-\epsilon}{3\pi}\right)(k_{ps} - k_{pcm})\right]\left[k_{pcm} + \frac{1-\epsilon}{3}(k_{ps} - k_{pcm})\right]}{k_{pcm} + \left[\frac{4}{3}\sqrt{\frac{1-\epsilon}{3\pi}}(1-\epsilon) + \pi\sqrt{\frac{1-\epsilon}{3\pi}} - (1-\epsilon)\right](k_{ps} - k_{pcm})} \quad (14)$$

On the other hand, the flowing HTF, in this case air, which absorbs the stored heat from the solidifying PCM is treated as an incompressible laminar Newtonian fluid and viscous heating is neglected. Furthermore, the inlet velocity of the HTF is constant while its inlet temperature varied with time. Referring to the general governing equations shown in Eq. (7), (8) and (9), the constant, **F** shown in Eq. (8) and (9) is taken to be zero for the HTF. In addition, looking at Eq. (9), the porosity, ϵ and the liquid fraction, γ are taken to be unity. This, basing on the HTF assumptions, reduces the general momentum and energy equations (Eq. (8) and (9)) to suite the HTF alone.

4.2. Boundary conditions

The domain shown in Fig. 13 is symmetrically subjected to numerical studies using the boundary conditions shown in Table 3. Referring to Table 3, regarding the experimental and numerical model comparison, a pure PCM case was used. Since the inlet and wall temperature profile varied with time, the boundary conditions were correlated from the experimental data. For the pure PCM case, the correlations are as shown in Eq. (15), (16) and (17). For the interface conditions, because of the thin wall thickness, the wall interaction with the HTF is neglected, so is the wall interaction with the PCM. It is, therefore, assumed that the HTF directly interacts with the PCM. In that regard, the interface boundary condition is taken to be that shown in Eq. (18).

$$T_i(t) = (3.0e-15t^4 - 2.0e-6t^3 + 3.0e-6t^2 - 0.0372t + 602.72) + 273.15 \quad (15)$$

$$T_o(t) = (1.0e-14t^4 - 6.0e-10t^3 + 8.0e-6t^2 - 0.05t + 676.52) + 273.15 \quad (16)$$

$$T_b(t) = (4.0e-15t^4 - 2.0e-6t^3 + 2.0e-6t^2 - 0.0191t + 601.82) + 273.15 \quad (17)$$

$$k_{htf}\frac{\partial T_{htf}}{\partial t} = k_{pcm}\frac{\partial T_{pcm}}{\partial t} \quad (18)$$

4.3. Numerical model validation

First of all, a suitable mesh size is paramount in obtaining an accurate prediction of the heat transfer phenomena in the PCM. For this purpose, the liquid fraction is used to understand the sensitivity of the mesh and the time step. Fig. 14(a) shows the liquid fraction comparison of 1.5 K, 2.5 K and 5 K mesh sizes for pure PCM experimental case. There is almost no noticeable difference in the results between the 1.5 K mesh size and the remaining two mesh sizes (2.5 K and 5 K). The major difference was that the 2.5 K and 5 K meshes met the set convergence criteria of 10^{-8}. Therefore, a 2.5 K mesh was chosen for this numerical study to obtain an accurate prediction of the heat transfer mechanism while at the same time minimising computational power. Also, a time step of 0.2 s was chosen after an independence test as shown in Fig. 14(b).

With the sensitivity study performed, a comparison of pure PCM experimental results to the numerical prediction is shown in Figs. 14(c) and 14(d). A reasonable agreement between experimental and numerical results is observed, particularly, the model is able to predict the first stage of sensible heat rejection and the overall time latent heat rejection takes place before a final sensible heat rejection is predicted. A mean absolute deviation between the experimental data and numerical prediction was calculated to be 5. The noticeable deviation during the early and last stage of sensible heat rejection can be attributed to the assumptions used in the model. For example, the model assumes a uniform wall temperature loss during the discharging process. However, basing on the experimental data, the outer wall temperature somewhat varies axially. Also, the numerical model assumes a perfectly uniform initial temperature at the start of solidification. However, looking at the experimental data, the initial discharging starting temperature is not uniform. The non-uniformity of the initial temperature can clearly be seen in thermocouples T09 and T07. This is attributed to the varying wall losses the experimental rig experiences during discharging. Furthermore, at a volumetric flow rate of 5 L/min of air, the inlet temperature to the numerical domain is derived from the experimental data and varies with time.

With the pure PCM experimental data and the numerical prediction results satisfactorily agreeing, the numerical model is then used to perform parametric studies. In the parametric studies, the HTF inlet temperature is fixed at 200 °C and the flow rate is varied from 5 L/min up to 30 L/min (the flow is still in laminar region) to observe the effect on solidification rate and heat transfer within the LTES system. Also, using the existing validated porous media models, a parametric study of the composite (PCM-periodic structure) case is performed to assess its performance if the periodic structure was additively manufactured as a connected tortuous tetrakaidecahedron periodic structure.

4.4. Numerical energy balance results

As mentioned in Section 3.3, a numerical study of the experimental control volume was performed by, first, accounting for the experimental heat losses and, second, assuming the control volume is fully adiabatic. With that, the temperature variation and the liquid fraction evolution with time within the control volume was reported for both the heat losses case and the adiabatic case. The difference in the total solidification time for both cases gives the overall lumped heat loss realised during experimental discharging. Basing on the numerical results shown in Fig. 15, particularly Fig. 15(b), about half of the energy was lost as heat losses to the surrounding. This scenario is expected at high temperature experimentation, where management of heat losses is a challenge, particularly if the surrounding environment temperature is not controlled.

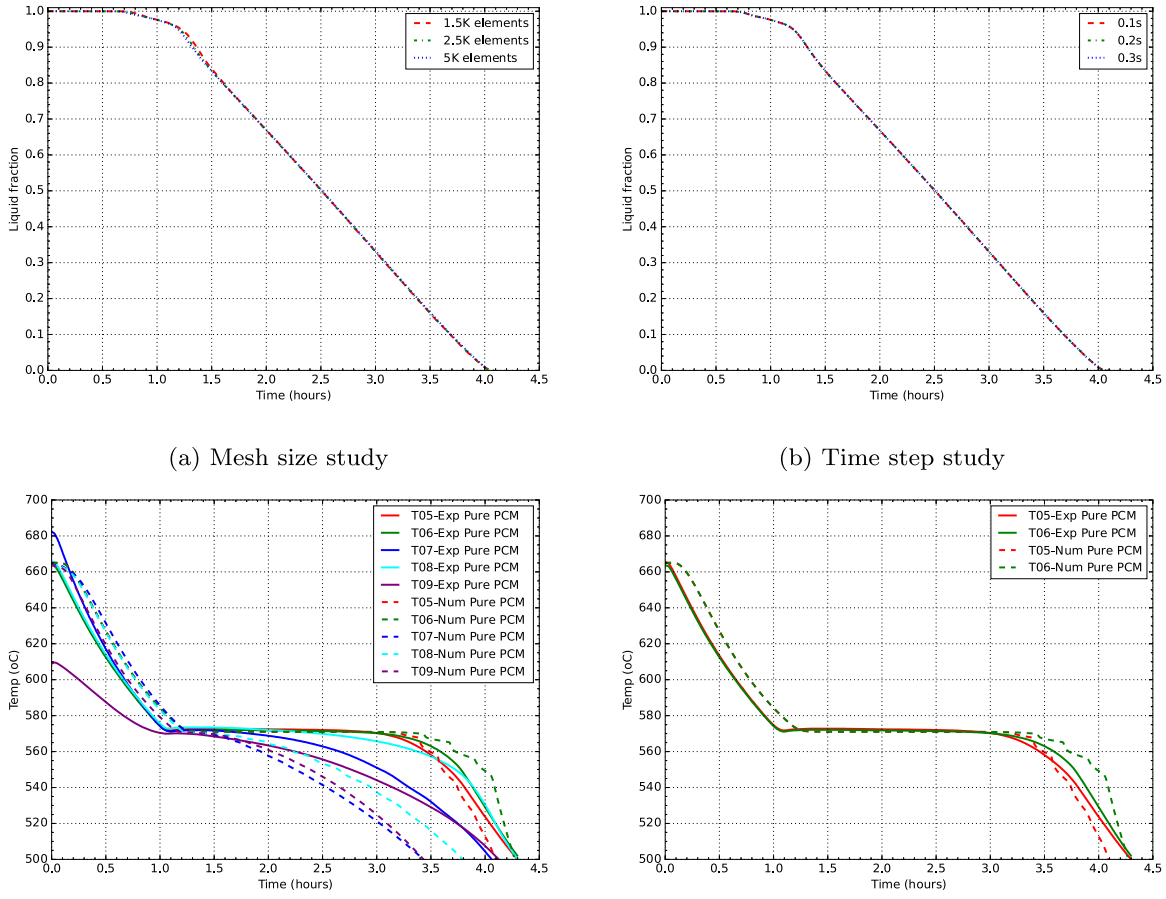

(a) Mesh size study

(b) Time step study

(c) Pure PCM case validation

(d) Pure PCM thermocouples within the PCM

Fig. 14. Numerical model validation using pure PCM experimental data.

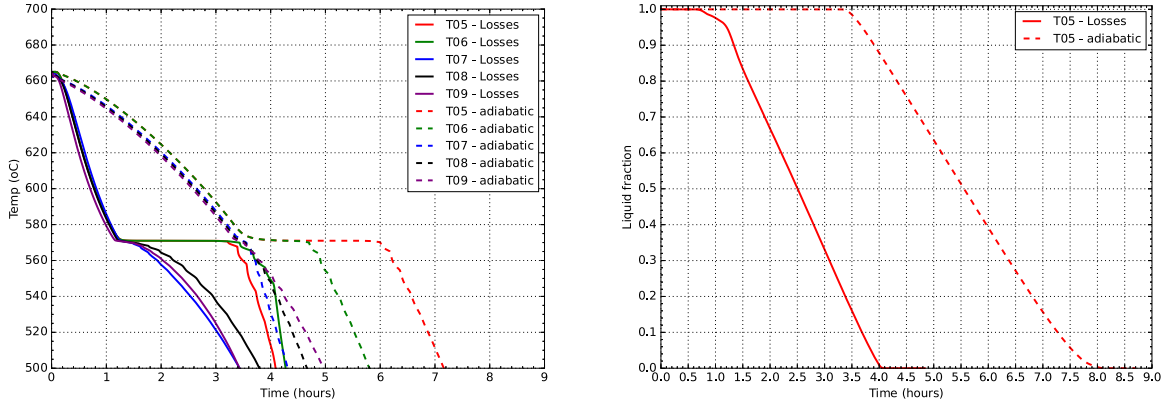

(a) Temperature with and without heat losses

(b) Liquid fraction with and without heat losses

Fig. 15. Estimation of the proportion of heat lost to the surrounding.

4.5. Numerical parametric studies

The discharging experiments were performed at a volumetric flow rate of 5 L/min (0.55 m/s) for both pure PCM and composite cases. The desire now is to show numerically how changing the air volumetric flow rate at a constant inlet temperature influences the solidification rate and the heat flux across the cooling wall. Fig. 16 shows that increasing the flow rate leads to a faster discharge as well as an increased heat flux to the HTF. The observed phenomenon demonstrates that increasing the HTF flow rate results to an increased temperature difference between the flowing HTF and the local temperature within the domain. The temperature difference, therefore, results in an increased heat flux across the cooling wall which leads to a faster decrease in

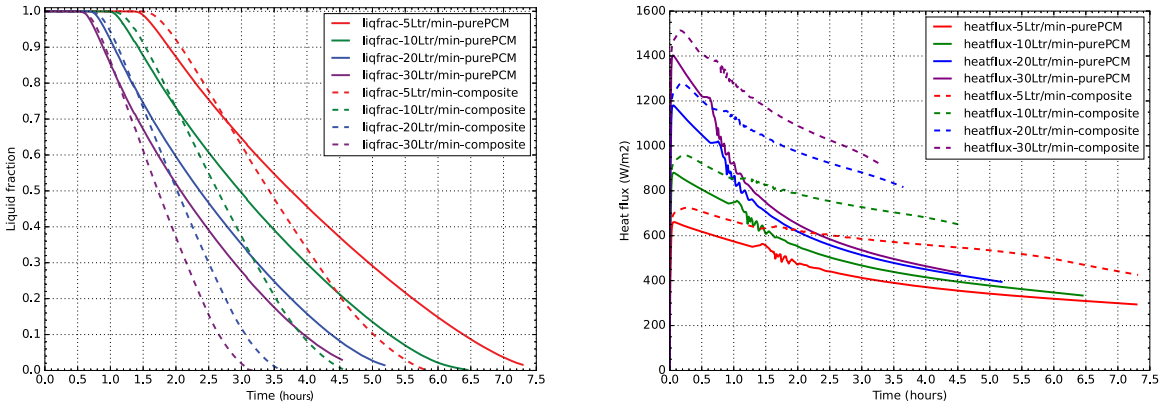

(a) Liquid fraction with varying air flow rate

(b) Heat flux with varying air flow rate

Fig. 16. Effect of the HTF flow rate for pure PCM and composite adiabatic cases.

temperature within the domain compared to cases when the HTF flow rate in low.

A closer look at the liquid fraction (see Fig. 16(a)) at various HTF flow rates for both pure PCM and composite cases shows that at a high liquid fraction, having a periodic structure does not speed the solidification process in the early sensible heat loss. The effect of having a periodic structure within the domain is realised when the liquid fraction is about 0.7. It is even evident in the last stage of sensible heat rejection. This is because, as the solidification process continues, the periodic structure enhances heat transfer within the solid regions due to the high thermal conductivity of the periodic structure. As the HTF flow rate increases, the enhancement effect of the periodic structure is noticed earlier in the first stage of sensible heat rejection. Overall, for HTF flow rates of 5 L/min, 10 L/min, 20 L/min and 30 L/min, the discharge time was shortened by 23%, 30%, 33% and 35%, respectively. A look at the heat flux rate across the wall (see Fig. 16(b)), it is observed that there is an immediate effect when the periodic structure is used compared to the case of pure PCM. This is expected since adding a periodic structure increases the heat transfer rate by conduction and thus an increased heat flux across the interface wall is realised. One notes that the fluctuations observed in the heat flux is noticed when a transition from liquid to solid is initiated. As this liquid fraction decreases with time, the heat flux across the wall stabilises.

In this regard, the choice of the discharging rate of the storage system can be obtained by choosing the appropriate HTF flow rate. Several factors have to be considered when choosing the right HTF flow rate such as the pipe sizing, the pumping capacity, the insulation requirements and so forth. It is, therefore, a decision that the designers come up with based on how fast the discharging process is required in the TES system.

A numerical visualisation of the solidification front for a pure PCM case during discharging was performed. A numerical visualisation of how the solidification front propagates when heat losses are accounted for and the case when the tank is fully adiabatic can be seen in Fig. 17. For the case of heat losses, the solidification front evolution (see Figs. 17(a) and 17(b)) is as expected where the liquid shrinkage occurs at the walls exposed to heat losses, that is the right wall, the bottom wall and the left wall of the tank where the HTF flows.

For the adiabatic case, on the other hand, the solidification front evolution (see Figs. 17(c) and 17(d)) is also as expected for a perfectly insulated wall, where the liquid shrinkage occurs at the left wall of the tank where the HTF flows. This occurs because as cooling air flows through the HTF pipe, the developing thermal layer and the gravitational pull results to solidification to accelerate at the area where a fully developed thermal layer is experienced.

5. Cost analysis

Here, we compare the material cost for both cases and present the benefits as faster charging and discharging processes. Assuming the experimental rigs were perfectly insulated for a temperature range of 450 °C–700 °C. The addition of wire screen has shortened the charging and discharging processes by 35% and 10%, respectively. Hence, the extra (material) cost is presented.

To estimate the cost of the metal screen, we calculate the mass of wire which fills the tank as shown in Fig. 13. With the outer diameter (D_o), the inner diameter (D_i), and the height (H) coupled with a given porosity ($\epsilon = 0.8$), one can determine the mass, m_{ss}, of the periodic structure used (see Eq. (19)). For the chosen metal screen used to make the periodic structure, the manufacturer provided weight per metre value of, $w_{ss} = 3$ kg/m. Therefore, the required length of the metal screen to make the periodic structure can be calculated using Eq. (20). When the calculated length is multiplied by the metal screen unit cost, $c_l = \$154$/m (see Eq. (21)), the periodic structure cost can be approximated as \$300. One can use different materials with higher conductivity but the corrosion will remain as a compatibility issue. If graphite foams were to be used instead, the cost would have been over 30 times higher (The cost for a graphite foam was about \$10,000 as per quote we received from industry providers). Hence, this paper offers a less expensive option for which the benefits (shorter cycles) are quantitatively presented.

$$m_{ss} = (1-\epsilon)\rho_{ss}\frac{\pi}{4}(D_o{}^2 - D_i{}^2) \tag{19}$$

$$L_{ss} = \frac{m_{ss}}{w_{ss}} \tag{20}$$

$$c_{ss} = c_l L_{ss} \tag{21}$$

6. Concluding remarks

In this study, a high temperature PCM that can be used in any high temperature application was used. The experiments were to demonstrate how metal inserts (periodic structures) made from readily available material can improve heat transfer within the TES system. The experimental results showed that inserting a loosely wrapped periodic structure into the PCM tank improves heat transfer and shortens the solidification process. Overall, it is observed that inserting the wire meshes improves the overall cycle performance by about 10%.

Furthermore, a numerical model was validated using the experimental data before a parametric study was performed. With the numerical model validated, a parametric study was performed to understand the effect of varying the HTF flow rate on the rate of heat transfer

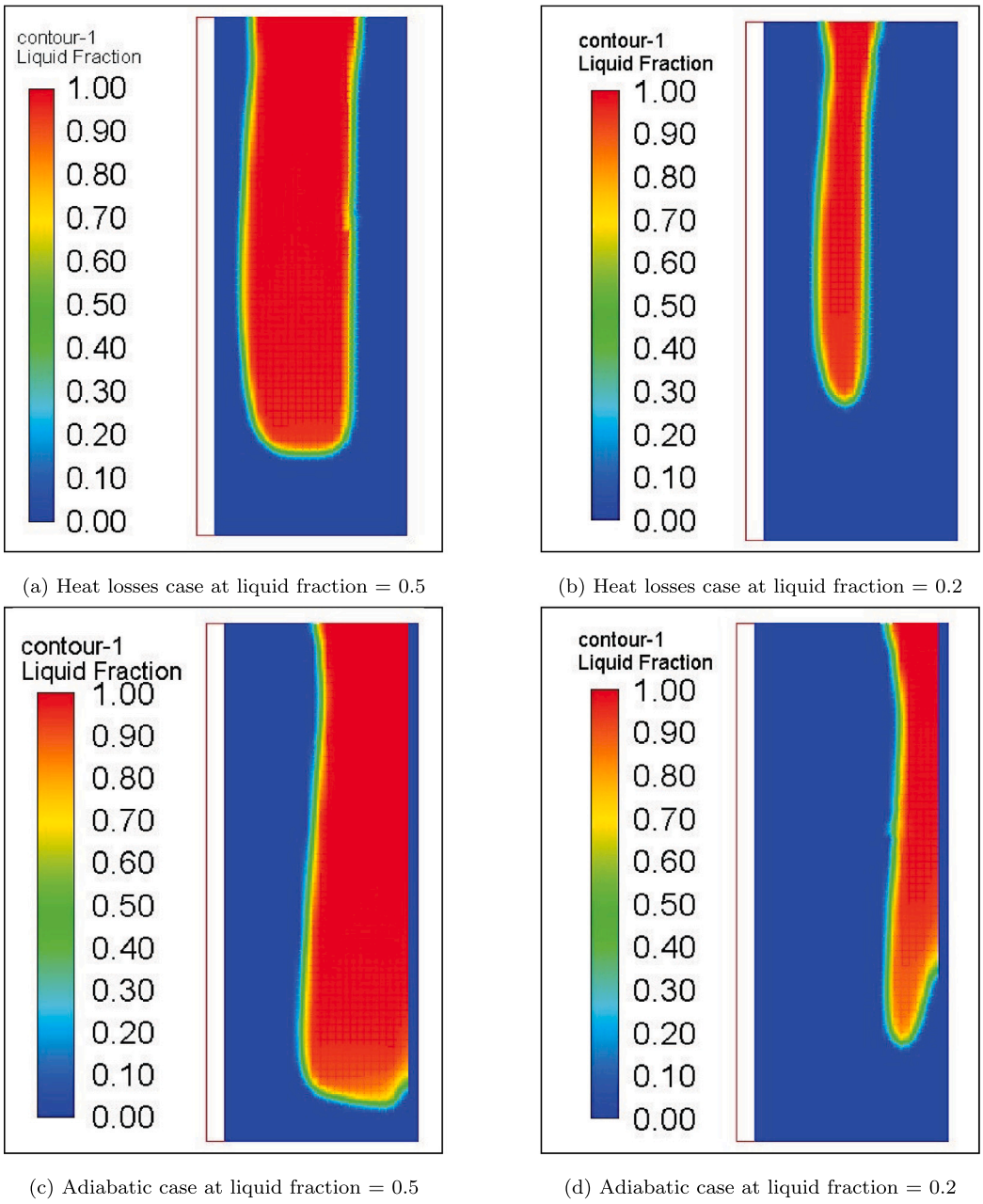

(a) Heat losses case at liquid fraction = 0.5

(b) Heat losses case at liquid fraction = 0.2

(c) Adiabatic case at liquid fraction = 0.5

(d) Adiabatic case at liquid fraction = 0.2

Fig. 17. Numerical visualisation of liquid fraction for both heat losses and adiabatic cases.

and the solidification rate. Results obtained showed that as the HTF flow rate increased, heat transfer was further enhanced and the total solidification time shortened. Overall, for HTF flow rates of 5 L/min, 10 L/min, 20 L/min and 30 L/min, the discharge time was shortened by 23%, 30%, 33% and 35%, respectively.

From the energy balance analysis, it is observed that about 50% of heat was lost to the surrounding. This, therefore, poses a heat loss management challenge during high temperature experiments. This however, could be improved by running experiments in a thermally controlled environment. This way, the rate of heat loss to the surrounding can be minimised due to the decreased temperature difference between the control volume local temperature and the surrounding temperature. In order to have a better understanding and thus gain confidence in using locally made periodic structures as heat transfer enhancement materials, experiments must be performed checking its performance in real operating conditions. The outlook of how this can be performed is presented below:

1. The periodic structure and the HTF pipe should have a perfect contact to minimise thermal contact resistance. This could be achieved through additive manufacturing or through welding and brazing.
2. The inherent heat loss management challenges during high temperature experimentation could be managed through performing experiments in a simulated testing environment. In this case, the surrounding temperature of the room could be controlled by heating the room to a desired surrounding temperature. This way, the temperature difference between the surrounding and the test rig internal local temperature is reduced and thus reducing heat losses to the environment.
3. The charging of the storage system could be performed from the centre of the test rig using a high resolution heating rod whose heat flux can be recorded in the data acquisition system. This way, heat losses to the surrounding can be minimised while at the same time the total energy input to the experimental rig is

collected in the data acquisition system. Also, the discharging process could be improved by using an industrial thermal oil as the HTF. This is because the thermophysical properties of the thermal oils will remain stable at a higher temperature compared to air.

4. At a lab scale, long term corrosion of the periodic structure could be assessed by running several charge–discharge cycles of the test rig. Once that is performed, the periodic structure material can then be characterised to observe how its corrosion rate varies with time. To improve the performance of the periodic structure, it could be coated with carbon based materials by depositing a thin layer of a non corrosive material, say, graphite. Although this approach might be intricate and comes at a cost, it is anticipated to be relatively cheaper as compared to using a full graphite foam as an enhancement material.

Declaration of competing interest

The authors declare that they have no known competing financial interests or personal relationships that could have appeared to influence the work reported in this paper.

Data availability

No data was used for the research described in the article.

Acknowledgements

This research was funded by the Australian Solar Thermal Research Institute (ASTRI), which is supported by the Australian Government, through the Australian Renewable Energy Agency (ARENA). The first author, Michael Opolot, would like to further thank the Australian Government for the Research Training Program Scholarship that enabled him to pursue this study. In addition, I would like to thank Lachlan Mudge for his unconditional support in fabricating and supporting in setting up the experiments. Frank Bruno and Ming Liu would also like to acknowledge the support received from the Australia India Strategic Research Fund (reference number AIRXII000124), Department of Industry, Science, Energy and Resources (Australia).

References

[1] Y. Lin, G. Alva, G. Fang, Review on thermal performances and applications of thermal energy storage systems with inorganic phase change materials, Energy 165 (2018) 685–708.
[2] M. Opolot, C. Zhao, M. Liu, S. Mancin, F. Bruno, K. Hooman, A review of high temperature (≥ 500°C) latent heat thermal energy storage, Renew. Sustain. Energy Rev. 160 (2022) 112293.
[3] A. Sharma, V.V. Tyagi, C. Chen, D. Buddhi, Review on thermal energy storage with phase change materials and applications, Renew. Sustain. Energy Rev. 13 (2) (2009) 318–345.
[4] B. Xu, P. Li, C. Chan, Application of phase change materials for thermal energy storage in concentrated solar thermal power plants: A review to recent developments, Appl. Energy 160 (2015) 286–307.
[5] M. Liu, W. Saman, F. Bruno, Review on storage materials and thermal performance enhancement techniques for high temperature phase change thermal storage systems, Renew. Sustain. Energy Rev. 16 (4) (2012) 2118–2132.
[6] D. Laing, T. Bauer, N. Breidenbach, B. Hachmann, M. Johnson, Development of high temperature phase-change-material storages, Appl. Energy 109 (2013) 497–504.
[7] C. Zhao, M. Opolot, M. Liu, F. Bruno, S. Mancin, K. Hooman, Numerical study of melting performance enhancement for PCM in an annular enclosure with internal-external fins and metal foams, Int. J. Heat Mass Transfer 150 (2020) 119348.
[8] M.M. Joybari, F. Haghighat, S. Seddegh, A.A. Al-Abidi, Heat transfer enhancement of phase change materials by fins under simultaneous charging and discharging, Energy Convers. Manage. 152 (2017) 136–156.
[9] A.M. Abdulateef, S. Mat, K. Sopian, J. Abdulateef, A.A. Gitan, Experimental and computational study of melting phase-change material in a triplex tube heat exchanger with longitudinal/triangular fins, Sol. Energy 155 (2017) 142–153.
[10] M. Hosseini, A. Ranjbar, M. Rahimi, R. Bahrampoury, Experimental and numerical evaluation of longitudinally finned latent heat thermal storage systems, Energy Build. 99 (2015) 263–272.
[11] W. Zhao, D.M. France, W. Yu, T. Kim, D. Singh, Phase change material with graphite foam for applications in high-temperature latent heat storage systems of concentrated solar power plants, Renew. Energy 69 (2014) 134–146.
[12] T. Kim, D.M. France, W. Yu, W. Zhao, D. Singh, Heat transfer analysis of a latent heat thermal energy storage system using graphite foam for concentrated solar power, Sol. Energy 103 (2014) 438–447.
[13] D. Singh, W. Yu, W. Zhao, T. Kim, D.M. France, R.K. Smith, Development and prototype testing of $MgCl_2$/graphite foam latent heat thermal energy storage system, Sol. Energy 159 (2018) 270–282.
[14] J.M. Mahdi, E.C. Nsofor, Multiple-segment metal foam application in the shell-and-tube PCM thermal energy storage system, J. Energy Storage 20 (2018) 529–541.
[15] X. Yang, W. Wang, C. Yang, L. Jin, T.J. Lu, Solidification of fluid saturated in open-cell metallic foams with graded morphologies, Int. J. Heat Mass Transfer 98 (2016) 60–69.
[16] J. Yang, L. Yang, C. Xu, X. Du, Numerical analysis on thermal behavior of solid–liquid phase change within copper foam with varying porosity, Int. J. Heat Mass Transfer 84 (2015) 1008–1018.
[17] S. Mancin, A. Diani, L. Doretti, K. Hooman, L. Rossetto, Experimental analysis of phase change phenomenon of paraffin waxes embedded in copper foams, Int. J. Therm. Sci. 90 (2015) 79–89.
[18] G. Righetti, R. Lazzarin, N. Marco, S. Mancin, Phase change materials embedded in porous matrices for hybrid thermal energy storages: Experimental results and modelling, Int. J. Refrig. (2019).
[19] G. Righetti, G. Savio, R. Meneghello, L. Doretti, S. Mancin, Experimental study of phase change material (PCM) embedded in 3D periodic structures realized via additive manufacturing, Int. J. Therm. Sci. 153 (2020) 106376.
[20] S. Ebadi, S.H. Tasnim, A.A. Aliabadi, S. Mahmud, An experimental investigation of the charging process of thermal energy storage system filled with PCM and metal wire mesh, Appl. Therm. Eng. (2020) 115266.
[21] A. Mustaffar, A. Harvey, D. Reay, Melting of phase change material assisted by expanded metal mesh, Appl. Therm. Eng. 90 (2015) 1052–1060.
[22] C. Zhao, M. Opolot, M. Liu, F. Bruno, S. Mancin, R. Flewell-Smith, K. Hooman, Simulations of melting performance enhancement for a PCM embedded in metal periodic structures, Int. J. Heat Mass Transfer 168 (2021) 120853.
[23] Y.-Z. Ling, X.-S. Zhang, F. Wang, X.-H. She, Performance study of phase change materials coupled with three-dimensional oscillating heat pipes with different structures for electronic cooling, Renew. Energy 154 (2020) 636–649.
[24] A. Ebrahimi, M. Hosseini, A. Ranjbar, M. Rahimi, R. Bahrampoury, Melting process investigation of phase change materials in a shell and tube heat exchanger enhanced with heat pipe, Renew. Energy 138 (2019) 378–394.
[25] A. Jamekhorshid, S. Sadrameli, M. Farid, A review of microencapsulation methods of phase change materials (PCMs) as a thermal energy storage (TES) medium, Renew. Sustain. Energy Rev. 31 (2014) 531–542.
[26] W. Li, R. Hou, H. Wan, P. Liu, G. He, F. Qin, A new strategy for enhanced latent heat energy storage with microencapsulated phase change material saturated in metal foam, Sol. Energy Mater. Sol. Cells 171 (2017) 197–204.
[27] F. Zhang, Y. Zhong, X. Yang, J. Lin, Z. Zhu, Encapsulation of metal-based phase change materials using ceramic shells prepared by spouted bed CVD method, Sol. Energy Mater. Sol. Cells 170 (2017) 137–142.
[28] A. Diani, L. Moro, L. Rossetto, Melting of paraffin waxes embedded in a porous matrix made by additive manufacturing, Appl. Sci. 11 (12) (2021) 5396.
[29] W.-D. Steinmann, D. Laing, R. Tamme, Development of PCM storage for process heat and power generation, J. Solar Energy Eng. 131 (4) (2009).
[30] R. Bayón, E. Rojas, L. Valenzuela, E. Zarza, J. León, Analysis of the experimental behaviour of a 100 kWth latent heat storage system for direct steam generation in solar thermal power plants, Appl. Therm. Eng. 30 (17–18) (2010) 2643–2651.
[31] D. Laing, T. Bauer, W.-D. Steinmann, D. Lehmann, Advanced high temperature latent heat storage system-design and test results, in: Effstock 2009, Abstract Book and Proceedings, 2009.
[32] C. Zhao, Z. Wu, Heat transfer enhancement of high temperature thermal energy storage using metal foams and expanded graphite, Sol. Energy Mater. Sol. Cells 95 (2) (2011) 636–643.
[33] C. Zhao, M. Opolot, M. Liu, F. Bruno, S. Mancin, K. Hooman, Phase change behaviour study of PCM tanks partially filled with graphite foam, Appl. Therm. Eng. 196 (2021) 117313.
[34] M. Opolot, C. Zhao, M. Liu, S. Mancin, F. Bruno, K. Hooman, Investigation of the effect of thermal resistance on the performance of phase change materials, Int. J. Therm. Sci. 164 (2021) 106852.
[35] A. Vasu, F.Y. Hagos, M. Noor, R. Mamat, W. Azmi, A.A. Abdullah, T.K. Ibrahim, Corrosion effect of phase change materials in solar thermal energy storage application, Renew. Sustain. Energy Rev. 76 (2017) 19–33.
[36] M. Liu, S. Bell, M. Segarra, N. Steven Tay, G. Will, W. Saman, F. Bruno, A eutectic salt high temperature phase change material: Thermal stability and corrosion of SS316 with respect to thermal cycling, Sol. Energy Mater. Sol. Cells 170 (2017) 1–7.

[37] M. Liu, E.S. Omaraa, J. Qi, P. Haseli, J. Ibrahim, D. Sergeev, M. Müller, F. Bruno, P. Majewski, Review and characterisation of high-temperature phase change material candidates between 500 C and 700°C, Renew. Sustain. Energy Rev. 150 (2021) 111528.
[38] W.S. Chang, Porosity and effective thermal conductivity of wire screens, Int. J. Heat Mass Transfer (1990).
[39] S.W. Churchill, H.H. Chu, Correlating equations for laminar and turbulent free convection from a vertical plate, Int. J. Heat Mass Transfer 18 (11) (1975) 1323–1329.
[40] J. Lloyd, W. Moran, Natural convection adjacent to horizontal surface of various platforms, Int. J. Heat Mass Transfer (1974).
[41] J. Xu, R.A. Wirtz, In-plane effective thermal conductivity of plain-weave screen laminates, IEEE Trans. Compon. Packag. Technol. 25 (4) (2002) 615–620.
[42] Y. Mahmoudi, K. Hooman, K. Vafai, Convective Heat Transfer in Porous Media, CRC Press, 2019.
[43] A. Brent, V. Voller, K. Reid, Enthalpy–porosity technique for modeling convection–diffusion phase change: Application to the melting of a pure metal, Numer. Heat Transfer 13 (3) (1988) 297–318.
[44] V.R. Voller, C. Prakash, A fixed grid numerical modelling methodology for convection-diffusion mushy region phase-change problems, Int. J. Heat Mass Transfer 30 (8) (1987) 1709–1719.
[45] V. Voller, M. Cross, N. Markatos, An enthalpy method for convection/diffusion phase change, Internat. J. Numer. Methods Engrg. 24 (1) (1987) 271–284.
[46] Z. Liu, Y. Yao, H. Wu, Numerical modeling for solid–liquid phase change phenomena in porous media: Shell-and-tube type latent heat thermal energy storage, Appl. Energy 112 (2013) 1222–1232.
[47] Y. Cao, A. Faghri, A numerical analysis of phase-change problems including natural convection, Trans. ASME (1990).
[48] V. Alexiades, A.D. Solomon, Mathematical Modeling of Melting and Freezing Processes, Hemisphere, Washington, D.C., 1993.
[49] D. Riley, F. Smith, G. Poots, The inward solidification of spheres and circular cylinders, Int. J. Heat Mass Transfer 17 (12) (1974) 1507–1516.
[50] K. Hooman, N. Dukhan, A theoretical model with experimental verification to predict hydrodynamics of foams, Transp. Porous Media 100 (3) (2013) 393–406.
[51] A. Tamayol, K. Hooman, Thermal assessment of forced convection through metal foam heat exchangers, J. Heat Transfer 133 (11) (2011).
[52] J.M. Mahdi, H.I. Mohammed, E.T. Hashim, P. Talebizadehsardari, E.C. Nsofor, Solidification enhancement with multiple PCMs, cascaded metal foam and nanoparticles in the shell-and-tube energy storage system, Appl. Energy 257 (2020) 113993.
[53] S.V. Patankar, Numerical Heat Transfer and Fluid Flow / Suhas V. Patankar., in: Series in computational and physical processes in mechanics and thermal sciences, Taylor & Francis, Boca Raton , FL, 1980.
[54] M. Opolot, C. Zhao, M. Liu, S. Mancin, F. Bruno, K. Hooman, Influence of cascaded graphite foams on thermal performance of high temperature phase change material storage systems, Appl. Therm. Eng. 180 (2020) 115618.
[55] P. Ranut, On the effective thermal conductivity of aluminum metal foams: Review and improvement of the available empirical and analytical models, Appl. Therm. Eng. 101 (2016) 496–524.
[56] O. Mesalhy, K. Lafdi, A. Elgafy, K. Bowman, Numerical study for enhancing the thermal conductivity of phase change material (PCM) storage using high thermal conductivity porous matrix, Energy Convers. Manage. 46 (6) (2005) 847–867.